Evaluating a new method of remote sensing for flood mapping in the urban and peri-urban areas: Applied to Addis Ababa and the Akaki catchment in Ethiopia

Tilaye Worku Bekele [a,b,c,*], Alemseged Tamiru Haile [a], Mark A. Trigg [d], Claire L. Walsh [e]

[a] International Water Management Institute (IWMI), P. O. Box, 5689, Addis Ababa, Ethiopia
[b] Africa Centre of Excellence for Water Management (ACEWM), Addis Ababa University, Addis Ababa, Ethiopia
[c] Water Technology Institute, Arba Minch University, P.O. Box 21, Arba Minch, Ethiopia
[d] School of Civil Engineering, University of Leeds, LS2 9JT, UK
[e] School of Engineering, Newcastle University, Newcastle upon Tyne, NE1 7RU, UK

ABSTRACT

The Sentinel-1 SAR dataset provides the opportunity to monitor floods at unprecedentedly high spatial and temporal resolutions. However, the accuracy of the flood maps can be affected by the image polarization, the flood detection method used, and the reference data. This research compared change detection and histogram thresholding methods using co-polarization (VV) and cross-polarization (VH) images for flood mapping in the Akaki catchment, Ethiopia, where Addis Ababa city is located. Reference data for the accuracy assessment were collected on the satellite overpass date. A new method, Root of Normalized Image Difference (RNID), has been developed for change detection. Multi-temporal flood maps using the best performing method and image polarization were generated from April to November of 2017–2020. Better accuracy was observed when using the RNID method on the VH polarization image with an overall accuracy of 95% and a kappa coefficient of 0.86. Results showed that flooding in the Akaki commonly begins in May and recedes in November, but flooding was most frequent and widespread from June to September. Irrigated land and built-up area accounted for 1057 ha and 544 ha of the inundated area, respectively. Several major roads in the study area were also affected by the floods during this period. Our findings indicate that the S-1 images were very useful for flood inundation mapping, the new change detection method (RNID) performed better in urban and peri-urban flood mapping, but the accuracy of the flood map significantly varied with the flood detection method and the image polarization.

1. Introduction

Ground-based monitoring of flood inundation is challenging due to site accessibility (Bayik et al., 2018), the rapidly varying nature of floods, and the limited capacity of national hydrological services, especially in low- and middle-income countries. However, remote sensing technologies can overcome these challenges to aid in Near Real-Time (NRT) monitoring of floods (Li et al., 2018a). In particular, radar satellites overcome the limitation of optical satellites for flood hazard monitoring at NRT conditions (Surampudi and Yarrakula, 2019). They can operate day and night and under all weather conditions (Zeng et al., 2020).

The Sentinel-1 (S-1) Synthetic Aperture Radar (SAR) is an active remote sensing (RS) satellite that records the signal backscatter intensity generated from the land surface (Devries et al., 2020). The S-1 data is available free of charge. Flood surfaces, under the radar, generate a specular (small) signal backscatter intensity that can be easily detected on an S-1 image (Conde & De Mata Muñoz, 2019). However, the small-signal backscatter from the flooded surface can be hidden by the double bounce (DB), dielectricity (blocking signal backscatter flow through the soil), and vegetation submerged during the flood (Mason et al., 2021; Tsyganskaya et al., 2018). These effects can cause the algorithm to miss actual floods. A steep topography affects the radar viewing angle, creating a shadow on the radar image (Zeng et al., 2020). Sandy areas produce low signal backscatter intensity similar to the flooded surface (Martinis and Plank, 2018). This causes false positive floods since the non-flood affected area can be detected as a flood. False floods can also be reported on the image by the effect of speckle noise (Conde & De Mata Muñoz, 2019).

The influence of the factors mentioned above can be large in highly heterogeneous urban areas (Chini et al., 2019; Liang and Liu, 2020). Consequently, reducing their effect on flood detection using the S-1 SAR dataset is an ongoing research challenge. For example, Li et al. (2019) applied the Interferometric (InSAR) coherence-based change to extract the flooded pixels from the phase difference observed between consecutive acquisition dates; their approach reduced errors caused by the DB. Tsyganskaya et al. (2018) implemented the Global Urban Footprint (GUF) dataset to mask the urban areas that can generate DB and, Anusha & Bharathi (2020) applied local thresholds to reduce the effects of heterogeneous land use in flood detection. Height above Nearest Drainage (HAND) and terrain slope masking have been applied to reduce the topography effect by masking the pixels situated on the high elevated and steep sloped areas (Clement et al., 2017).

Based on the level of user involvement in training the algorithm, the flood mapping methods using the S-1 SAR dataset can be categorized as automatic (Liang and Liu, 2020), semi-automatic (Andreoli and Yesou, 2007) and manual (Zhang et al., 2020). These three methods may use either multi-temporal S-1 dataset (a reference and flooded image), e.g. change detection, Red Green Blue (RGB) composition methods (Conde & De Mata Muñoz, 2019); or single (target) image (Schlaffer et al., 2015) analysis using histogram thresholding, fuzzy logic, regional growing, texture analysis as listed in (Clement et al., 2017) to detect the flooded pixels.

Histogram thresholding is a widely used method for flood mapping due to its flexibility, simplicity, and effectiveness (Gumma et al., 2020). The bi-modal histogram of signal backscatter intensity is expected from the combination of flooded and non-flooded surfaces. A threshold is identified at the intersection of the two overlapping histograms to distinguish the backscatter intensity generated from the flooded and non-flooded land surfaces. The pixels with signal backscatter intensity less than the threshold value are categorized as the flooded pixels. To simplify the estimation of the threshold value, Liang & Liu (2020) divided their study area into many small parts to make sure that the analysis area proportionally covered the water and land surfaces. Tavus et al. (2018) and Manjusree et al. (2012) determined the average signal backscatter intensity generated from different water bodies to optimize the value of a flood threshold. However, determining the threshold is challenging due to the small flood depth at the interface of the flooded and non-flooded surface that may affect the signal backscatter intensity.

In the change detection method, dual images are acquired from a dry season (reference) and flooded (target) images to detect signal backscatter intensity changes between the two conditions. The maximum change is found at the interface of the flooded and non-flooded area (Clement et al., 2017). Hence the change detection method is combined with thresholding and other clustering algorithms to detect the flooded (target) pixels (Tavus et al., 2018). The image difference (Clement et al., 2017; Long et al., 2014), image rationing (Andreoli and Yesou, 2007), and log-ration (Bayik et al., 2018; Li et al., 2018a) are the most commonly used methods due to their ease of detection of the land surface changes obtained from the reference and target images (Long et al., 2014). By using dual image methods, the permanent sandy area, DB, shadow and layover generated from both reference and flooded images have minimum effect when detecting the flooded pixels (Li et al., 2018a). However, the selection of the reference image affects the performance of the change detection method for flood inundation mapping (Schlaffer et al., 2015). Nevertheless, optimal difference and a reduced soil moisture effect are obtained when applying a flood free reference image (Li et al., 2018a). For instance, Hostache et al. (2012) determined the non-flooded reference image based on the irregularity index observed on the histogram of signal backscatter intensity of the radar image. A suitable reference image has low irregularity index. Based on statistical analysis, the image which contains close to the median backscatter intensity of all the candidate images can be selected as the better reference image in flood detection (Clement et al., 2017; Hostache et al., 2012). However, the median value of the signal backscatter intensity of the

candidate images can be affected by different factors. Tavus et al. (2018) and Reksten & Solberg (2019) randomly selected the reference image acquired before the flood (target) image. These studies did not evaluate the effects of the reference image on the accuracy of the flood map. Hence, the flood inundated area may be over or underestimated because of the selected reference image.

The accuracy of a flood map can be determined qualitatively (Long et al., 2014) and some studies did not report the accuracy of the flood map they generated (Ganji et al., 2019; Tavus et al., 2018). Most studies applied a secondary dataset, for instance, optical satellite image (Clement et al., 2017; Long et al., 2014), modelled flood map, land cover map, community information (Dadhich et al., 2019), or Ground Control Points (GCPs) collected from GeoEye-1 high-resolution airborne imagery to validate the S-1 dataset for flood mapping (Zeng et al., 2020; Schlaffer et al., 2015). These secondary datasets can introduce additional errors that are not present in the S-1 dataset at the Near Real-Time condition. For instance, Kianfar (2019) used Sentinel-2 (S-2) optical satellite images acquired two days before S-1A and four days after S–1B. Martinis & Plank (2018) collected the optical satellite image that was acquired five days later than the S-1 overpass. Hence, the time difference between the acquisition of the S-1 and the secondary reference data introduces additional errors in evaluating flood map accuracy. Some studies reported the accuracy, but did not report the various error components to determine whether false or missed floods caused the primary error. For instance, Liang & Liu (2020) reported high overall accuracies of greater than 97% with better detection accuracy of non-flooded surface than the target flooded area. Zeng et al. (2020) obtained 89.9% overall accuracy and kappa coefficient of 0.681.

The main objective of this study is the evaluation and comparison of methods and image polarizations of the S-1 SAR dataset for flood extent mapping in urban and peri-urban areas applied to the Akaki catchment that feeds the Awash Basin of Ethiopia. The Akaki has a large economic significance for the country given the location of the capital city, Addis Ababa. The evaluation of the different methods is performed using in-situ data collected on the date of the satellite overpass. We also evaluate the spatial and temporal variability of flood occurrence from April to November of 2017–2020, to determine the flood affected major roads in the Addis Ababa city and flooded Land Use Land Cover (LULC) classes in the Akaki catchment.

2. Material and methodology

2.1. Description of the study area

The Akaki is a catchment of the Upper Awash River sub-basin. Addis Ababa city, which is experiencing a rapid growth, is situated in the Akaki catchment. Three water supply reservoirs (Dire, Legedadi, and Gefersa) are located in the upstream part, and the Aba Samuel reservoir (hydropower plant) is situated at the outlet of the catchment (Fig. 1). The Akaki has a catchment area of about 1500 km^2 with an elevation range from 2,028 m (a.m.s.l) to 3,370 m (a.m.s.l). The average terrain slope of the Akaki catchment is 10.6%, with 25% of the catchment area steeply sloping (8–15% slope).

Two main rivers, which are the Big Akaki and Little Akaki, drain the Akaki catchment to feed the Aba Samuel reservoir. The main tributaries of Big Akaki River are the Bulbula and Kebena rivers, with the former draining the north-east peri-urban part of the catchment and the latter draining the north part of the catchment (the old part of the Addis Ababa city). The Bulbula River is fed by the Legedadi River from its most upstream part, which hosts the small towns of Dire, Legedadi and Sendefa. The flood release from the Legedadi and Dire reservoirs is conveyed by the Legedadi River towards the Bulbula River and then towards the floodplain of the Big Akaki River. The Little Akaki River drains the northwest part of the catchment. It conveys water released from the Gefersa reservoir towards the floodplains and then feeds the Aba Samuel reservoir.
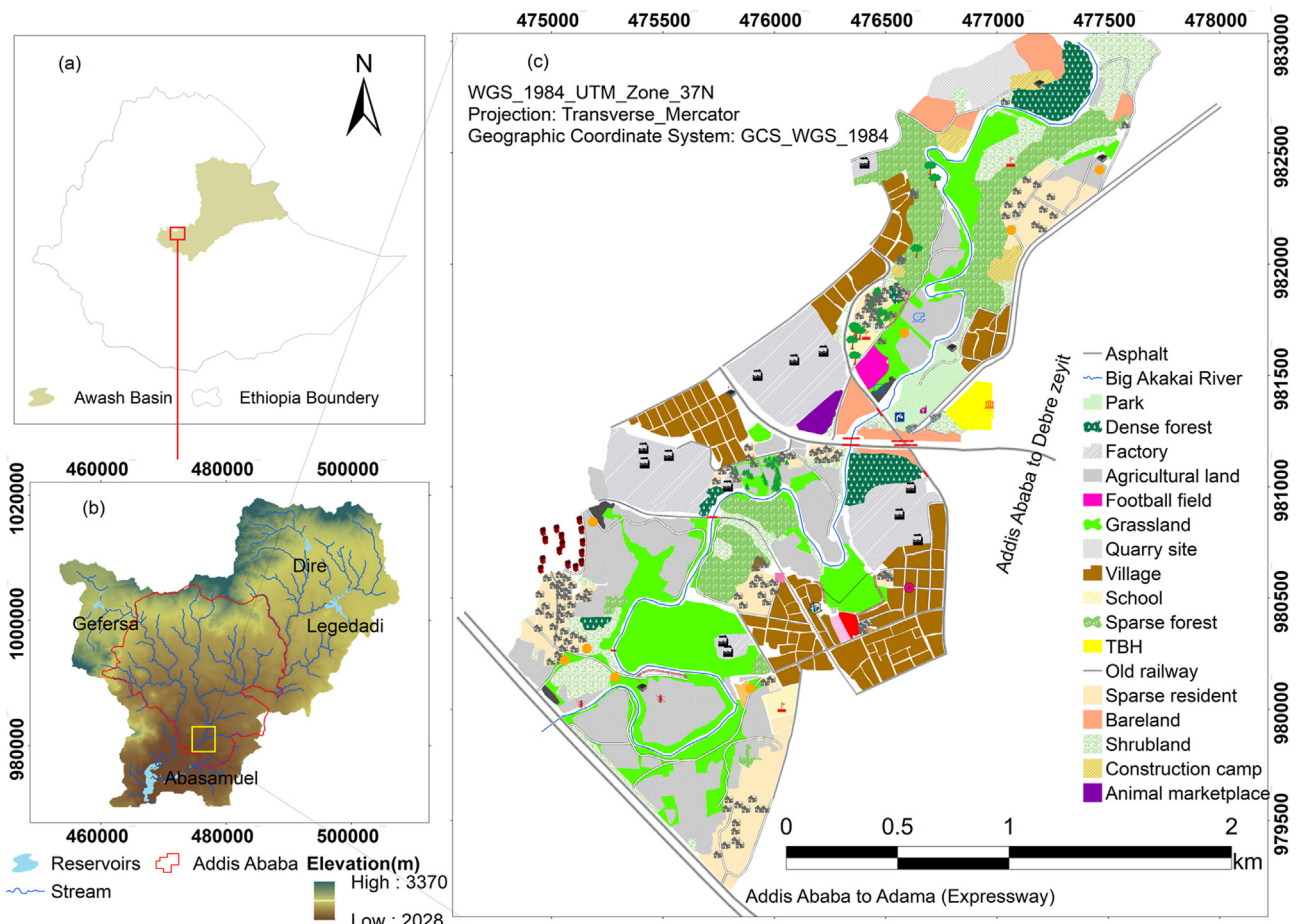
Fig. 1. Location map of the study area: - (a) the boundary of Ethiopia and Awash River basin, (b) the elevation, and drainage of the Akaki catchment where the Addis Ababa city is located (red polyline), and (c) detailed base map that is digitized from Google Earth imagery and GPS tracking of features at the downstream flood-prone area of the catchment around Tirunesh Beijing Hospital (TBH).

The Akaki catchment has seven main land use land cover (LULC) classes: built-up area, rainfed-agricultural, irrigated agricultural, bare land, grassland, mixed forest, and water body. A large part of the catchment is covered by the rainfed agricultural land (33.98% of the catchment area) and the built-up area accounts for 25.55% of the catchment area. The detailed area coverage of each LULC class within the Akaki catchment is shown in Table 1. The asphalt roads, resident, commercial, industrial, and paved land are categorized as built-up area due to the similarity in their hydrological response (runoff generation). The irrigated land is mostly found at the downstream stretches of both the Little and Big Akaki Rivers. The method used to detect the land cover classes is described in section 2.5.

The main wet season (called Kiremt) of the Akaki catchment is only four months, June to September whereas, the Belg (small rainy season) is from mid-February to April. The catchment receives the maximum

monthly rainfall (250 mm–300 mm) in July and August. The mean annual rainfall of the catchment is 1254 mm. For further details on the climate of the Akaki catchment, reference is made to Risi et al. (2020); Demlie et al. (2007).

2.2. Datasets

In this study, 80 pre-processed (for thermal and border noise removal, radiometric calibration, orthorectification and georeferencing) S-1 SAR images were accessed and analyzed in Google Earth Engine (GEE). These images were acquired from April to November of 2017–2020 for multi-temporal flood extent mapping. The S-1 satellites were launched on April 3, 2014 (S-1A) and April 25, 2016 (S–1B). S-1A and S–1B are positioned at a 180° phase difference to operate over the land surface with 6 day intervals over Europe (Li et al., 2018a), but at 12 day intervals for the rest of the earth surface (Devries et al., 2020). The S-1 dataset is employed in different image modes: Interferometric Wide swath (IW), Stripmap (SM), Extra-Wide swath (EW), and Wave Mode (WM). The IW S-1 dataset is suitable for land observation and flood monitoring (Conde & De Mata Muñoz, 2019). It has a wide swath of 250 km, with a resampled spatial resolution of 10 × 10 m. Based on the direction of the transmitted microwave radiation and reception of the signal backscatter intensity, the IW dataset has different combinations, co-polarization (vertical transmit-vertical receive, VV) and cross polarization (vertical transmit-horizontal receive, VH) (Kianfar, 2019).

The Sentinel-2 (S-2) optical image satellite was launched by the European Space Agency (ESA). Its two missions are S-2A, launched on June 23, 2015 and S–2B, launched on March 7, 2017. S-2A and S–2B are

Table 1
LULC classes of the Akaki catchment as classified using the Sentinel-2 image.

LULC classes	Land Use Land Cover (LULC)	
	Area (ha)	(%) of Akaki catchment
Rainfed agriculture	50,034	33.98
Built-up	37,616	25.55
Bare land	8217	5.58
Forest area	19,247	13.07
Grassland	26,277	17.85
Irrigated	4965	3.37
Water Body	869	0.59

positioned at 180° phase difference. These satellites have 12 spectral-bands at a 10–60 m horizontal resolution (Nguyen et al., 2020). Both satellites have a revisit interval of 5 days over non-equatorial regions.

We obtained the roads network map of the Addis Ababa city from the OpenStreetMap data sources https://extract.bbbike.org/.

We used the Global Surface Water (GSW) dataset to mask the permanent surface water bodies from the S-1 image. GSW was developed by the Joint Research Center (JRC) of the European Commission using all Landsat image available in GEE. The GSW was developed from 3,865,618 scenes of the Landsat 5, 7, 8 satellite, with a 30 m resolution covering March 16, 1984 to the present. The images were classified into water and non-water bodies using change detection approaches applied between the time periods of 1984–1999 and 2000–2016 (Pekel et al., 2016).

A 10m horizontal spatial resolution DEM and administrative boundaries of the sub-areas of Addis Ababa city were collected from the Ethiopia Geospatial Information Institute (EGII). The DEM was generated by a photogrammetry technique with Ground Sampling Distance (GSD) of 25 cm and the maximum expected vertical accuracy is double the GSD (50 cm) (Personal communication with the EGII staff). The elevation dataset was used to mask the pixels situated on steep sloping areas to discard false alarms during flood detection from the S-1 image (Clement et al., 2017; Zhang et al., 2020).

2.3. Methods

Ground Control Points (GCPs) were systematically collected from the flooded and non-flooded surface areas to evaluate the accuracy of the flood inundation maps that were generated using the S-1 dataset. To match the S-1 image resolution, the GCPs were collected from a minimum flood inundated area of 10×10 m. However, the GCPs for the non-flooded area were collected at the edge of the flooded area and at a distance 10–30 m (up to 3 pixels) further from the edge of the flooded surface. The flood extent of September 9, 2020, which was also the satellite overpass date of S-1, was found to be large enough, and hence was used for validation of the flood inundation map that was extracted from the S-1 image. In this study, 233 GCPs were collected on September 9, 2020 (179 GCPs from flooded and 54 GCPs from non-flooded surface). In addition, 433 GCPs were collected from six different land cover classes in December 2020 to evaluate the accuracy of LULC map that was generated from the S-2 dataset by using machine learning algorithms in GEE.

JavaScript was used to implement the algorithm in GEE and an Application Programming Interface was used to access, process and detect floods from the S-1 dataset (Mutanga & Kumar, 2019). The GCPs collected from the field at the date of the satellite overpass were used to evaluate the accuracy of the flood maps detected from the S-1 image. We compared the change detection and histogram thresholding methods for flood detection. Both methods were applied separately with the VV and VH polarization of the S-1 datasets. However, speckle noise is a common problem to overcome before using the S-1 SAR dataset for flood detection. Here, we used the median statistical method in a small window size of 3×3 to minimize the effect of high signal backscatter variability and to prevent information loss from important features. This median filter method is not influenced by the extreme signal backscatter intensity generated from the flooded surfaces (Andreoli and Yesou, 2007; Bhatt et al., 2017).

2.3.1. Flood inundation mapping

For the histogram thresholding method, the signal backscatter intensity generated from a single target (flooded) image was analyzed to detect the flood affected pixels by applying a threshold value. Two histograms of signal backscatter intensity are expected from the S-1 image collected in the flood season, (i) a histogram of signal backscatter intensity generated from the land surface (containing high signal backscatter intensity) and (ii) a histogram of signal backscatter intensity generated from the land surface (containing high signal backscatter intensity). Then, the flood threshold value that was located inside the

intersection of the two histogram peaks was used to distinguish the flooded and non-flooded surface pixels. However, due to the non-proportional area coverage of the flooded and non-flooded area that was obtained at the date of S-1 satellite overpass (September 9, 2020) in the Akaki catchment, the generated histogram was dominated by the signal backscatter intensity of the non-flooded surface. Hence, firstly we estimated the threshold value from the literature (Ganji et al., 2019; Bhatt et al., 2017; O'Hara et al., 2019). Then, the threshold value was adjusted based on the expert knowledge of the boundary between the flooded and non-flooded area as observed during the field visit on the date of the satellite overpass. Therefore, the flood threshold value was adjusted until an optimal threshold value and an acceptable accuracy are obtained with reference to the GCPs collected and until the pattern of the flood map resembles what was observed in the field. The method was applied separately for co-polarization (VV) and cross-polarization (VH) of the S-1 dataset. The accuracy of the flood maps generated from the two polarizations was compared using an error matrix.

In this study, a new change detection method called the root of normalized image difference (RNID) was developed to retain the characteristics of the S-1 radar sensor in the flooded pixel. The previous change detection methods (Clement et al., 2017) can detect changes in all features during the time-period between the acquisition date of the reference image and the target image. Thus, the methods may not isolate the change by flooding from the changes by other factors. This led to the generation of additional false flood alarms. The limitation of these previous change detection methods in reporting false flood alarms can be overcome by the RNID method which is developed based on the assumptions that feature that generate false flood alarms can be identified and eliminated by using dry and wet season images. It is assumed that the pixels of the S-1 image affected by flooding have lower signal backscatter intensity than the pixels of the dry season (reference) image. Therefore, only the pixels of the target image which have a lower signal backscatter intensity than the reference image can be detected as flooded.

The following steps were used when applying the RNID method. First, the flood (target) image (I2) was collected from the flooded season. The reference image (I1) was then selected by following the method applied in (Hostache et al., 2012). The candidate reference images were acquired for the driest month i.e. January of 2017–2020. Then the image contains minimum irregularity index and has a small signal backscatter variability was selected as the reference image. The irregularity index is used to determine the variety of a pixel's signal backscatter intensity value from the given image (Hostache et al., 2012). It is determined by the difference between 95% and 5% inferred pixel's signal backscatter intensity values of the image. From the common characteristics of the S-1 dataset, the image from the flooded period has a large signal backscatter variability (i.e. large irregularity index) relative to the image of the dry period, since the signal backscatter intensity generated from the flooded pixels greatly varies from that generated from non-flooded pixels.

Two different reference images that contained a minimum irregularity index were selected to evaluate the effects of the reference image on the accuracy of flood inundation maps. These reference images were selected (i) from the candidate images that contained a minimum irregularity index from January of 2017–2019 and (ii) January of 2020 that was acquired from the same year as the target image. Therefore, in this study, we selected the dry period image that has minimum irregularity index as a reference image to detect flooded pixels using the change detection method. The threshold was identified at the start of the high signal backscatter variability observed on the histogram of the RNID values to distinguish the flood affected pixels. The RNID equation reads: -

$$RNID = \left(\frac{I1 - I2}{I1 + I2}\right)^{0.5} \qquad\qquad 3.1$$

where: - RNID is a change detection method developed in this study, *I1* is the signal backscatter intensity of the reference (dry) season image, and *I2* is the signal backscatter intensity of the flooded (target) image.

To select the best performing polarization of the S-1 data, the method was applied separately for co-polarization (VV) and cross-polarization (VH). The error (confusion) matrix was used to evaluate the accuracy of the resulting flood inundation maps. The error matrix contains n x n cells (rows and columns), where n is the number of land cover classes. The column contains the GCPs of the land cover classes, and the row contains the classified data using the satellite image. The diagonal elements in the matrix indicate the number of correctly classified pixels, whereas the non-diagonal element indicates the number of incorrectly classified pixels. The overall accuracy, producer's accuracy, and user's accuracy were determined from the matrix (Zeng et al., 2020). Additionally, the agreement between the GCPs (reference data) and the classified flood data was determined by the statistical analysis of the kappa coefficient (Rwanga and Ndambuki, 2017; Nkomeje, 2017).

2.3.2. Multi-temporal flood mapping and analysis

Flooding occurs dynamically throughout a certain time duration, whereas the satellite provides instantaneous data (snap-shot) at a regular time interval. Hence, the satellite can miss flood information between the acquisition dates, particularly with rapid urban flooding. However, the multi-temporal nature of satellite data over long periods can provide an adequate sample size to characterize the flood extent (Martinis and Plank, 2018; Trigg et al., 2013). In the Akaki catchment, flooding commonly occurs in the main rainy season from June to September. However, it might occasionally extend outside the rainy season. The flood inundation maps were generated from April to November of 2017–2020 (4 years) by using the best performing method and polarization of the S-1 dataset. The frequency of flood occurrence was estimated for each pixel to show the seasonal and inter-annual flood variations. The flooded pixels were categorized as 'rarely', 'sometimes', 'moderately', 'mostly' and 'always' affected by flooding. These categories were determined as follows: (i) a binary map was generated for each image acquired in the analysis period with a value of 1 indicating flooded pixel and 0 indicating non-flooded pixel; (ii) frequency of flood occurrence was estimated by aggregating (through addition) of the binary maps over the analysis period; and (iii) a frequency value classes were applied to categorize the flood affected pixels into the five flood occurrence frequency classes. For this study, the pixels were categorized as follows: "always affected" when the flood occurrence exceeds 90% of the time; "mostly affected" when the flood occurrence is between 60% and 90%; "moderately affected" when the flood occurrence is between 40% and 60%; "sometimes affected" when the flood occurrence is between 10 and 40% of the time; and "rarely affected" if the flood occurrence is less than 10% of the time. To show the spatial-temporal frequency of flood occurrence the domain area selected was at the downstream of the study area as it is frequently affected by flooding.

2.3.3. Land use land cover (LULC) classification

The pre-processed S-2A level-2A dataset was used to generate a LULC classification dataset with UTM/WGS84 projection/datum. The European Space Agency (ESA) develop and provide the Sentinel-2 tool-box that can be used to pre-process the S-2 dataset. Already, pre-processed and atmospherically corrected to obtain the bottom atmosphere reflectance (BOA), the S-2 image dataset was loaded into GEE (Verde et al., 2020). We mapped the irrigated land using the image acquired during the irrigation season and other land cover classes including the rain-fed agricultural land were mapped using the image which was acquired during the rainy season. The two maps were merged using overlay analysis to enhance the accuracy of the LULC map. A supervised classification was applied using the machine learning algorithms offered in the GEE platform. The Classification And Regression Tree (CART), Naive-Bayes and Support Vector machine (SVM) algorithms are commonly used for LULC classification (Nguyen et al., 2020). The accuracy of these algorithms was evaluated with GCPs as a reference and by using an error matrix to select the best performing. The GCPs were collected from six different land cover classes during the field trip to the catchment.

However, the LULC map detected from the S-2 dataset does not capture the detail of roads that exist in the Akaki catchment and Addis Ababa city.

2.3.4. Flood exposure assessment

The flood exposure of the major roads of Addis Ababa city and the LULC classes of the study area were also assessed. During the field work to collect the GCPs, many streets were flooded in Addis Ababa city due to the extreme rainfall.[1] The poor performance and blocking of the city's drainage system is one of the major reasons for the occurrence of this street flooding. This flash flooding usually lasts between a few minutes to hours and occasionally for a few days. The S-1 SAR satellite's ability to capture such flood affected roads is evaluated. The flood occurrence maps that were detected from the S-1 image were overlaid on the Google earth image to visually identify the flood affected roads. However, the flood occurrence map was intersected with OpenStreetMap data using overlay analysis in GIS, to determine the length of flood affected roads in Addis Ababa city.

3. Result and discussion

In this section, the results are presented and interpreted for: (i) the accuracy of the flood maps generated using the two methods as separately applied to two polarizations of the S-1 data, (ii) the frequency of flood occurrence in the Akaki catchment from April to November of 2017–2020 and, (iii) the flood affected roads in Addis Ababa city and the different LULC classes in the Akaki catchment.

3.1. Accuracy assessment

The accuracy of flood inundation maps that was detected using histogram thresholding method on the S-1 VH polarization data was determined using error matrix. These flood maps were detected by applying different threshold values which are (−20 dB, −21 dB, −22 dB, and −25 dB) as shown in Fig. 2. The flood extents and their accuracies varied for each threshold value. Varying the threshold values caused the overall accuracy of the flood map to vary from 85 to 88% and the kappa coefficient varied from 0.66 to 0.71. The optimal threshold value is found as −21 dB as it produced an overall accuracy of 88% and kappa value of 0.71. The error matrix for the best performed threshold value (−21 dB) was presented in this study, the detailed description is presented in the next paragraph.

Table 2 shows the accuracy of the flood inundation map that was detected using the histogram thresholding method on the VH polarization data. The optimal flood threshold value was estimated as −21 dB, which resulted in the highest accuracy. The histogram thresholding method has a user accuracy of 87.7% for the flooded pixel and 90.7% for the non-flooded pixels as shown in Table 2. This indicates that 87.7% of the flooded pixels on the map are flooded as observed on the ground. We observed the largest commission error at the boundary of the flooded and non-flooded surface and where the flood-depth is low (<20 cm). Whereas, 96.91% of the flooded area on the ground was identified as flooded on the satellite derived map (producer's accuracy = 96.91%) and a high omission error was observed in the non-flooded surface. Generally, the accuracy of flood inundation maps that were generated using the histogram thresholding method on the VH polarization can be rated as moderate.

The accuracy of the flood inundation map which was detected using histogram thresholding method applied on the VV polarization data is shown in Table 3. The optimal threshold value was determined as −15 dB that resulted in the best accuracy. It shows that 74.3% of the flooded pixels detected on the map matched with the actual flood on the ground. A high commission error was observed near the interface of the flooded
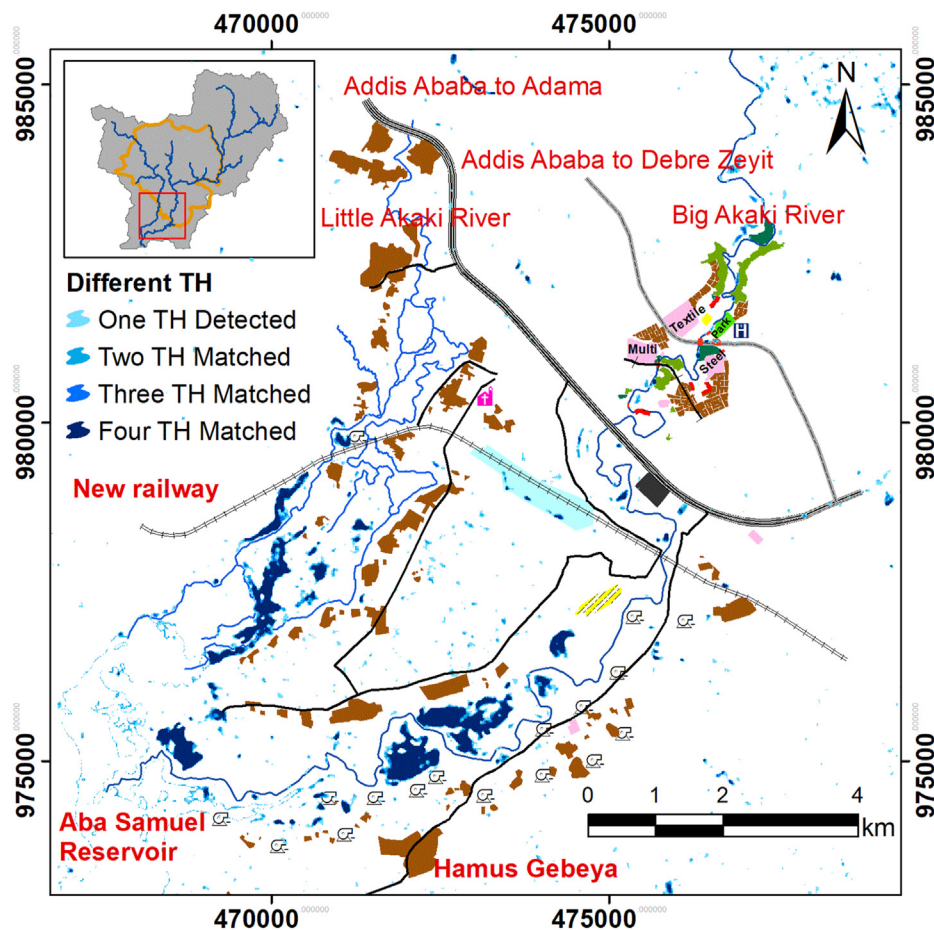
---

[1] https://www.tobiatube247.com/article-read.php?a=1313.

Fig. 2. The flood inundation maps detected using the method of Histogram thresholding (HT) by applying various threshold values. In the legend, "One …" indicates the flooded pixels were detected only when one of the threshold values was specified, "Two …" indicates detection by two of the threshold values, and so forth.

Table 2
Error matrix of the flood inundation map of 9 September 2020 using the VH polarization and the histogram thresholding method.

Classified	Reference data (GCPs)				
	Flooded	Non-flooded	Σ	User's accuracy	Commission error
Flooded	157	22	179	87.7%	12.3%
Non-flooded	5	49	54	90.7%	9.3%
Σ	162	71	233		
Producer's accuracy	96.91	69.01			
Omission error	3.09	30.99			

Table 3
Error matrix of the flood inundation map of September 9 2020, which was produced by using VV polarization and the histogram thresholding method.

Classified	Reference data (GCPs)				
	Flooded	Non-flooded	Σ	User's accuracy	Commission error
Flooded	133	46	179	74.30%	25.7%
Non-Flooded	3	51	54	94.44%	5.56%
Σ	136	97			
Producer's accuracy	97.79%	52.58%			
Omission error	2.21%	47.42%			

surface and the non-flooded surface that have a shallow flood depth.

Most of the flooded pixels on the ground were detected as the flooded surface on the satellite map (producer's accuracy = 97.7%). High omission error was found in the non-flooded surface since the reference GCPs collected from the small flood depth were detected as non-flooded. The overall accuracy of the flood map which was generated using the histogram thresholding method on the VV polarization data is 79% and the kappa coefficient is 0.53.

The change detection (RNID) method requires two satellite images (reference and target or flooded image) to detect the flooded area. Here we identified 10 images from the driest month (January) from 2017 to 2020 as a candidate reference image. However, the irregularity index was found to be at a minimum for the reference image of January 6, 2019. For the sake of comparison, we also used the image of January 25, 2020, which has the minimum irregularity index in 2020, as a reference image.

Fig. 3 shows the flood inundation maps detected using the RNID method by applying these two different reference images to evaluate its impact on the flood inundation maps. There is a moderate difference observed between the flood map generated using the two reference images, with a large difference observed for small flood extents.

Table 4 shows the error matrix of the flood map generated using the change detection method on the VH data with the January 6, 2019 reference image. The flood map has a user accuracy of about 95% for the flooded pixel and 94% for the non-flooded pixels. This is equivalent to a commission error of only 6%. There was a large difference on the producer's accuracy of the non-flooded (85%) and flooded (98.3%) pixels, with higher accuracy for the latter. The overall accuracy of the flood map is 95%, with a kappa statistic coefficient of 0.86, which indicates strong agreement between the classified and reference dataset. Generally, the
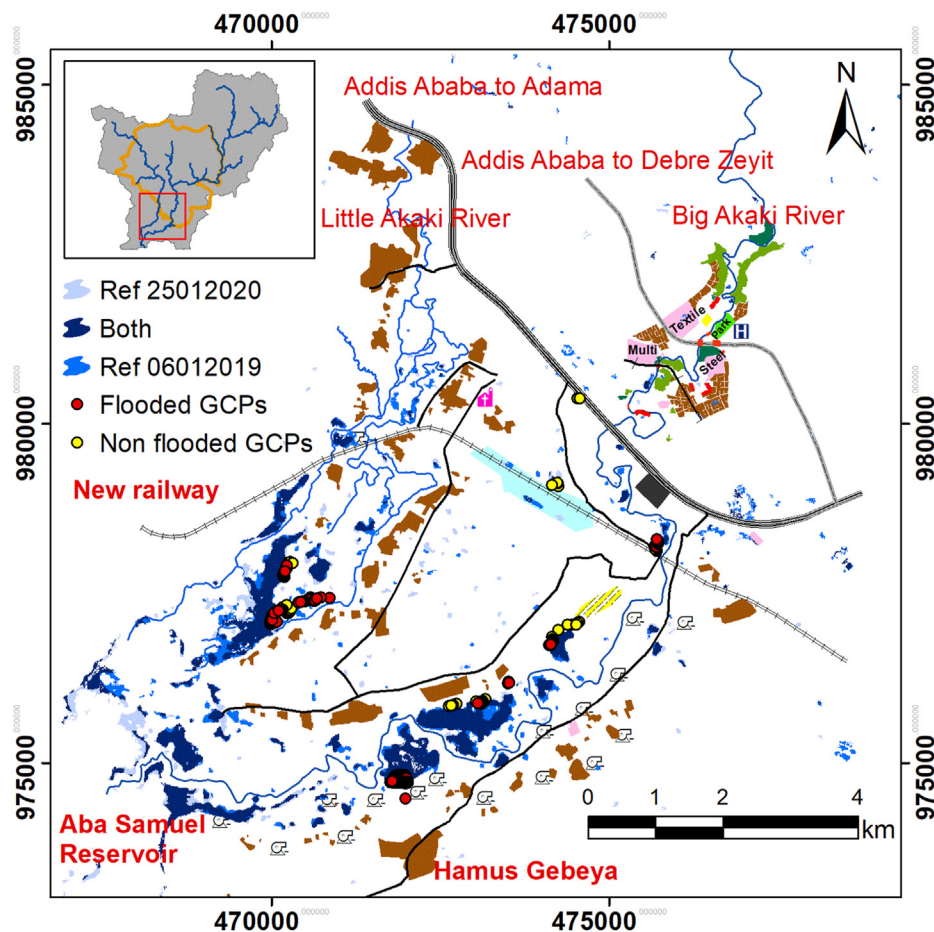
Fig. 3. September 9, 2020 flood inundation maps detected using two different reference images acquired on January 25, 2020 and January 6, 2019. In the legend, "Both" represents pixels are detected as flooded when applying both reference images, whereas "Ref 06012019" and "Ref 25012020" represent floods detected by the respective reference images.

Table 4
Error matrix of the flood inundation map of September 9 2020 by using the method of change detection (Root of Normalized Image Difference) on the VH polarization and image of January 6 2019 as reference.

Classified	Reference data (GCPs)				
	Flooded	Non-flooded	Σ	User's accuracy	Commission error
Flooded	170	9	179	94.97%	5.03%
Non-flooded	3	51	54	94.4%	5.56%
Σ	173	60	233		
Producer's accuracy	98.3%	85%			
Omission error	1.7%	15%			

Table 5
Error matrix of the flood inundation map detected using change detection (Root of Normalized Image Difference) method on the VV polarization of S-1 dataset.

Classified	Reference data (GCPs)				
	Flooded	Non-flooded	Σ	User's accuracy	Commission error
Flooded	152	27	179	84.9%	15.1%
Non-Flooded	4	50	54	92.6%	7.4%
Σ	156	77			
Producer's accuracy	97.4%	64.9%			
Omission error	2.6%	35.1%			

overall accuracy of the flood inundation maps that were produced using the RNID method on the VH polarization was greater than 95% and that can be rated as almost perfect (Rwanga and Ndambuki, 2017). Whereas, by comparison, applying the January 25, 2020 reference image result in an overall accuracy of 94% and kappa coefficient of 0.84.

Table 5 shows the accuracy of flood inundation map produced by the RNID method applied to the VV polarization data. The producer's accuracy is low (64.9%) for the non-flooded area and the omission error is 35.1%, which indicates that most of the flooded pixels on the ground were detected as non-flooded in the map. The GCPs which are characterized by shallow depths (<20 cm) were detected as non-flooded area. The user accuracy is 84.9% which indicates that the flooded pixels detected on the map mostly matched with the flood affected pixels on the ground. The overall accuracy of the flood inundation map is 86.7% and

kappa coefficient is 0.67. For the RNID method applied to the VV polarization data, this indicates only a moderate agreement between the classification and what is on the ground during the flood event.

3.2. Flood occurrence

Flood inundation maps were generated for the flood season from April to November over four years (2017–2020) using the best performing method (i.e. RNID method), VH polarization data and the image of January 06, 2019 as the reference image. The following sub-sections describe the interpretation of the maps.

3.2.1. Frequency of flood occurrence

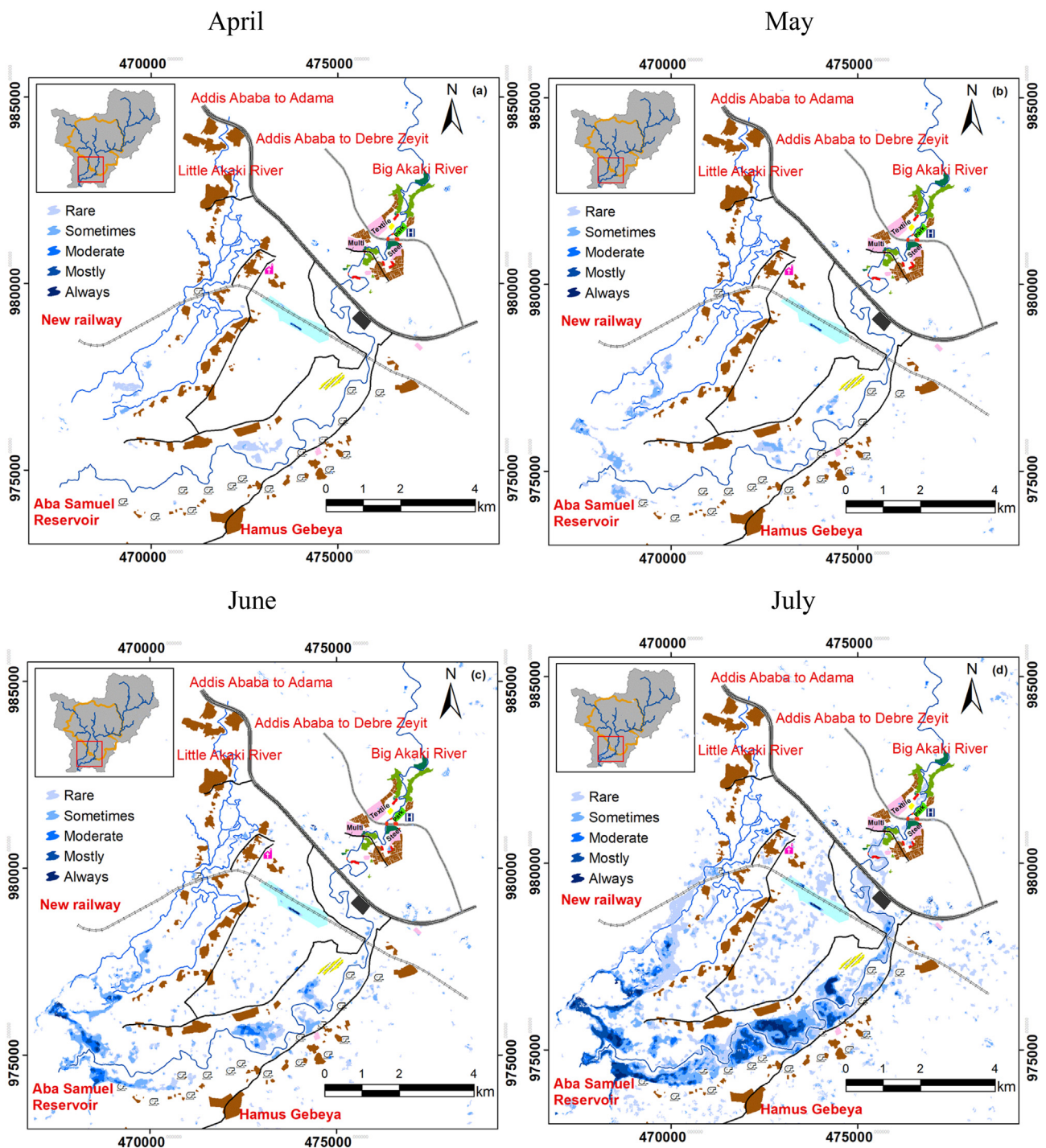In Fig. 4A and Fig. 4B, the frequency of flood occurrence is shown for

Fig. 4(A). Monthly frequency of flood occurrence maps detected in April (a) to July (d) from 2017 to 2020 left to right sequence shown at the downstream of the catchment.

the flood season that stretches from April (left top) to July (right bottom) and August (left top) to November (right bottom) of 2017–2020, respectively. We focused mainly on the downstream part of the catchment where flooding is frequent and widespread, as observed during the field visit. In April, the flood extent was small and concentrated close to the Aba Samuel reservoir. In May, small size flooded pockets started to appear along the Little Akaki and Big Akaki rivers. The flood pockets then connected to form a more extensive flooded surface in June. Small pluvial floods were also detected in the area situated between the Big and Little Akaki River. In July, the flood extent increased by a large amount compared to that of the earlier months. The flood stretched along the Big

Akaki riverside from the Tirunesh Beijing Hospital (TBH) to the Aba Samuel reservoir. Additionally, an increased extent of pluvial flood was observed in the area between the Big and Little Akaki riversides. Frequent flooding was detected in the area that is situated downstream of Kilinto prison. Along the little Akaki riverside the flood extended from the area around the new railway (rare flood) to the Aba Samuel reservoir (frequent flood). Near the new railway, the residents and their livestock were affected by the flood that occurred in July.

In August, the riverine and pluvial floods contracted compared to the flood extent of July. Still frequent floods were observed inside the meandering section of the Big Akaki river which is situated downstream
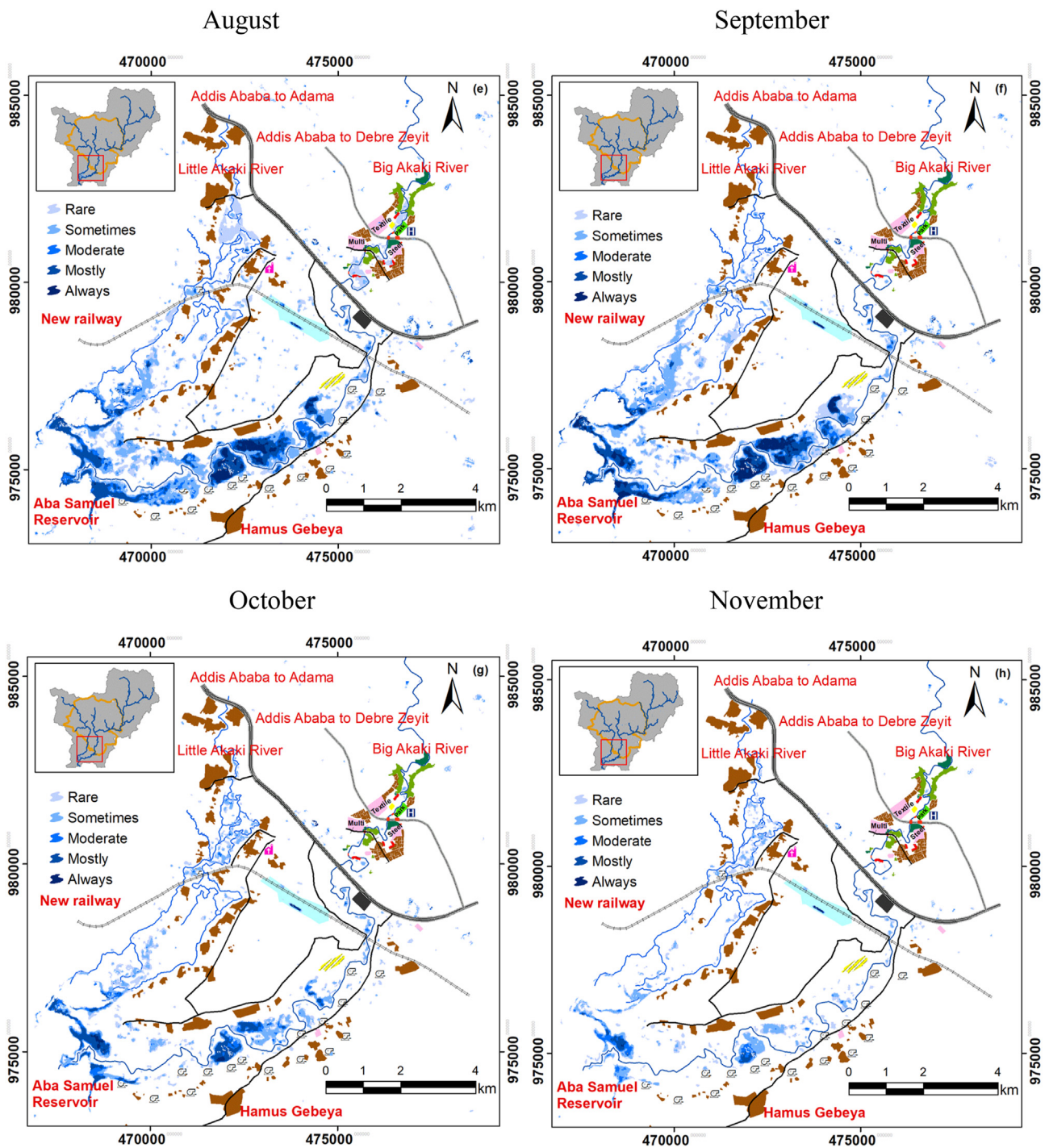
Fig. 4(B). Monthly frequency of flood occurrence maps detected in August (e) to November (h) from 2017 to 2020 left to right sequence shown at the downstream of the catchment.

of the rail station. Rare flooding was detected along the Little Akaki riverside. However, frequent flood affected areas were observed at the most downstream parts which are situated close to Aba Samuel reservoir. In September, the pluvial flood which was observed in the previous month disappeared and the inundation extent decreased along the Big and Little Akaki rivers. A low frequency flood still occurred at the new railway along the downstream stretch of the Little Akaki River. In October, new flood areas were not detected, whereas the existing riverine and pluvial flooding were highly reduced along both Big and Little Akaki

riversides. The floods of Akaki catchment receded in November except for small flood pockets inside the deepest and meandering section of the river.

Fig. 5 shows inter-annual flood extent variability that was detected per twelve-day interval of S-1 overpass time from April to November of 2017–2020. In the Akaki catchment, a large flood extent was detected on July 22, 2018 which inundated 0.6% of the total catchment area. There was also a large flood in June 2018 which covered 0.39% of the catchment area, whereas an unusual large flood extent was observed in
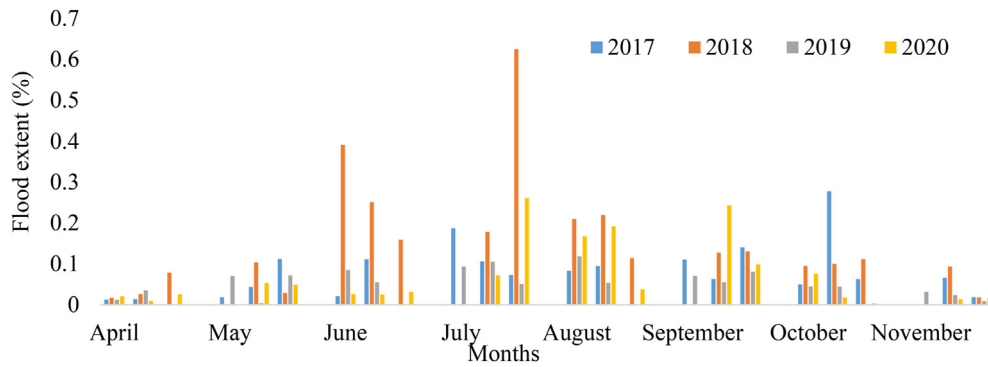
Fig. 5. Temporal variation of the flood extent in the Akaki catchment detected from April to November of 2017–2020.

October 2017, which is outside the main rainy season. The flood extent in July and August 2020 covered 0.26% and 0.19% of the Akaki catchment area, respectively.

The flood occurrence frequency map for the period from April to November of 2017–2020 is shown in Fig. 6. Most of the inundated area was observed downstream of the Addis Ababa to Adama expressway. During a visit to the study area in the summer of 2020, we observed that the community's mobility and their livestock were highly affected by these floods. Along the Big Akaki river, the pumps, which are used to deliver drinking water to the city, are shown in the map. These pumping sites are prone to flooding particularly in terms of affecting access to the sites. Most parts of the flooded surface were affected by rarely occurring floods. However, areas in the meandering section of the river were affected by frequently occurring floods.
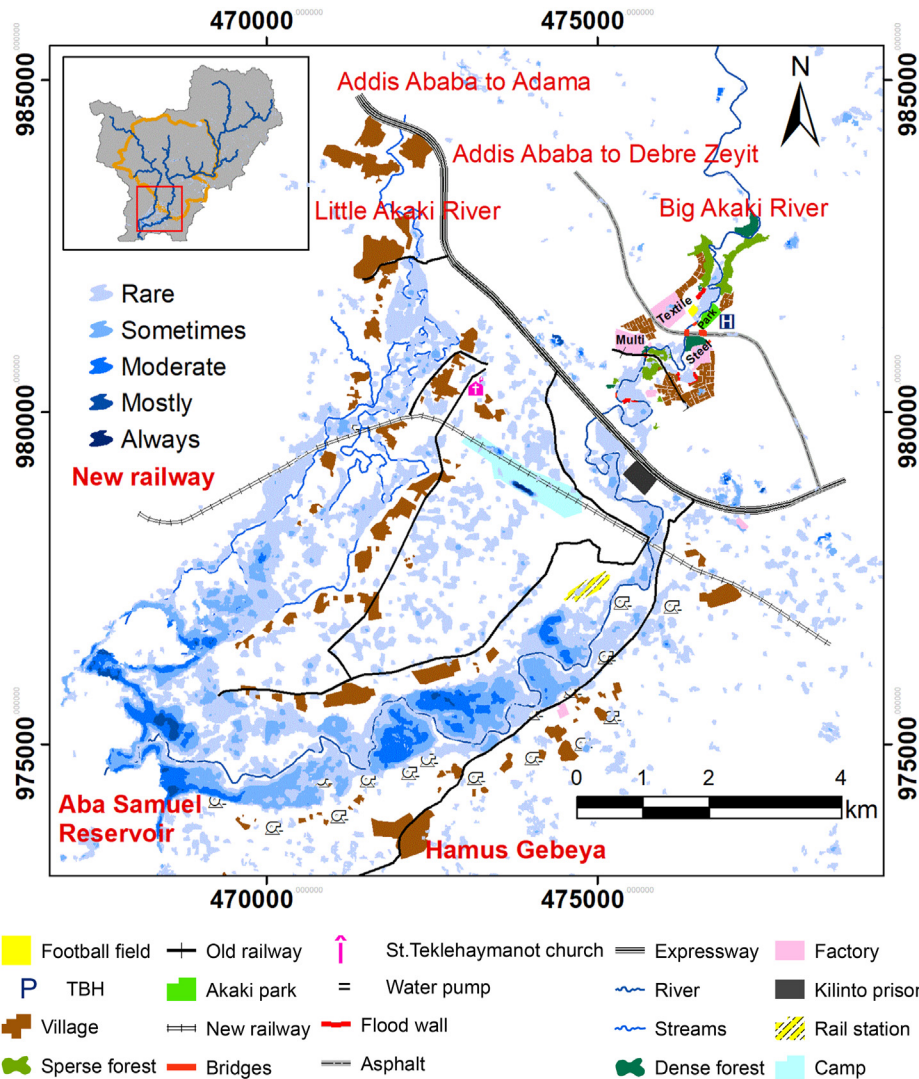

Fig. 6. Flood inundation extent and frequency of flood occurrence at the downstream part of the Akaki catchment. The analysis period is from April to November of 2017–2020. See the legend of Fig. 2 for the features on the map.

3.3. Flood affected roads and LULC classes

The S-1 images were used to identify the flood affected roads in Addis Ababa City. For instance, roads in the Gurd Shola area (around ILRI campus), from Lebu Mebrat Hail to Jemo-1 (around the Safeway supermarket) (Fig. 7A), Maseltegna to Kality (around Wiha Limat) and from Michael taxi Mazoriya to Jemo-1 (around Anbesa Garaj) (Fig. 7B) were identified as flood affected roads. We were also able to identify several major roads of Addis Ababa city that were affected by rare to frequently floods.

The road map shows that the total length of roads in Addis Ababa city is 5002 km. These roads are categorized into different classes based on the standard grades. The flood inundation map generated in this study indicates that 2.2% (108 km) of the roads were affected by floods in the analysis period of this study. Table 6 shows the length of major roads (trunk, track, primary, secondary, tertiary) and different LULC classes that were inundated by the flood. During flooding, most roads of Addis Ababa are congested with traffic, affecting mobility. These roads are also affected by flooding which necessities major maintenance work after each rainy season, not only by extreme rainfall but also by inadequate and poor management of the drainage system of the city and its road network.

The CART algorithm performed better for LULC classification of the Akaki catchment, and hence was used for the classification. The dominant LULC classes in the Akaki catchment are rainfed agricultural land (34% of the total Akaki catchment area) and built-up area (25.78% of the total Akaki catchment area). The local farmers informed us that an unexpected early flood in the irrigation season causes losses of standing crops. Our finding also indicates about 1057.05 ha irrigated land was affected in the Akaki (Table 6). A large part of the built-up area (544.11 ha) was affected by flooding between 2017 and 2020. We observed that the impact of flooding in the built-up areas is widespread and requires further future investigation. It is also noted that 209 ha of the rainfed agricultural land was affected by flooding. Some farmers informed us that they no longer practice rainfed agriculture since the frequency of flood inundation of their farmland significantly increased in recent years.

3.4. Discussion

For both methods of flood mapping (RNID change detection and histogram thresholding), a better accuracy was obtained when using the VH polarization than the VV polarization data. This finding is similar to the finding of (Conde & De Mata Muñoz, 2019). The VV polarization has two limitations: (i) it does not detect flooded areas with shallow depth and generates as high a signal backscatter intensity as the non-flooded surface, which leads to underestimation of the flood affected area
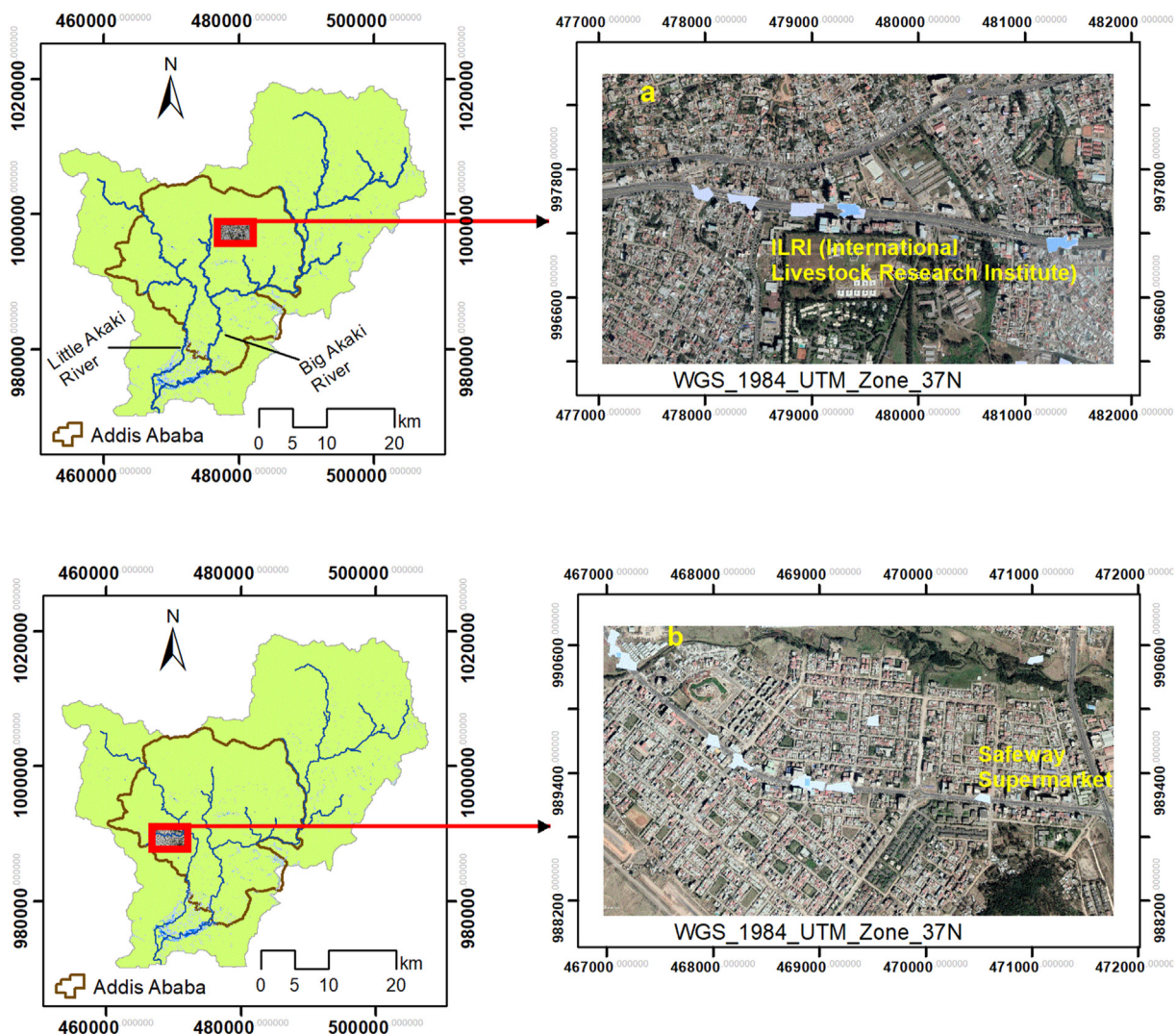

Fig. 7 (A). Some of the major roads in Addis Ababa city that were affected by floods. These roads are, Megenagna to Gurd Shola road (a), from Lebu Mebrat Hail to Jemo-1 road (b). The Google Earth satellite image was used as a background.
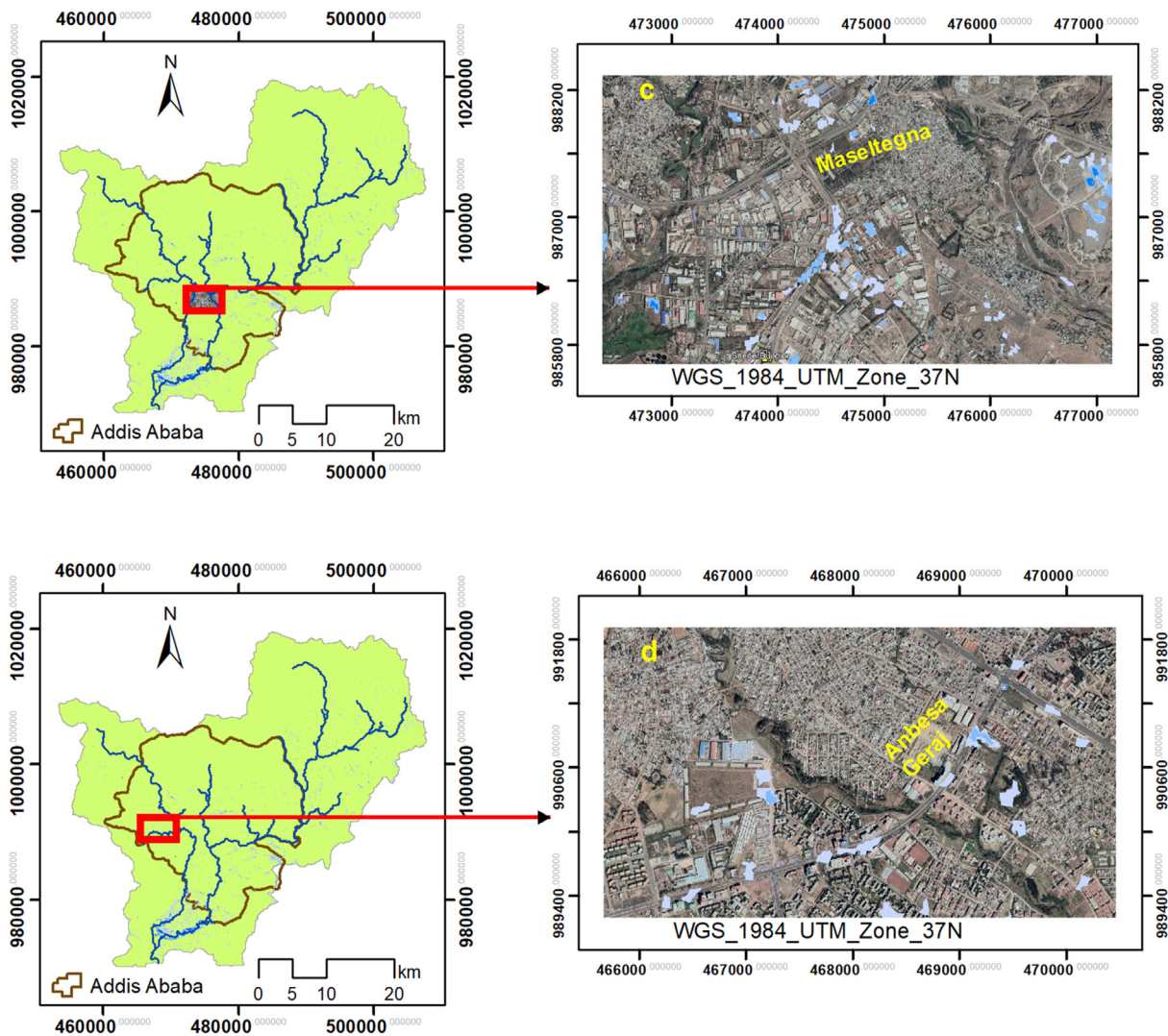
Fig. 7 (B). Some of the major roads in Addis Ababa city that were affected by floods. These roads are from Maseltegna to Kality (C) and from Michael taxi mazoriya to Jemo-1 (D).

Table 6
Length of major road types and area of land cover classes affected by flood from 2017 to 2020. Inundated land cover classes were determined as area in percentage (%) of individual land cover classes.

Road type	Length(m)			Flood Inundation
Primary	1424.7	Land cover classes	Area (ha)	Inundated part of the LULC area (%)
Primary link	20414.8	Rainfed agriculture	208.53	0.42
Secondary	28899.4	Built-up	544.11	1.44
Secondary link	1888.6	Bare land	147.99	1.8
Tertiary	22.3	Forest area	73.31	0.38
Tertiary link	7658.1	Grassland	281.69	1.07
Track	30.8	Irrigated	1057.05	21.28
Trunk	2154.6			
Trunk link	6916.2			

(Clement et al., 2017); and (ii) it can result in false positive flood detection since its low incidence angle allows penetration of moist sparse soil to generate dark pixels on the S-1 image incorrectly identified as a flooded surface (Bayik et al., 2018; Gumma et al., 2020). When using the change detection method in this study, the VV polarization resulted in 511.37 ha of flood extent, whereas the VH polarization data resulted in 256.23 ha of flood extent in the Akaki catchment. This indicates false flood alarms are more dominant than flood misses when using the VV polarization for the Akaki catchment. Known non-flooded farmlands were wrongly detected as flooded inundated surface on the date of September 9, 2020 satellite overpass.

The optimal threshold value used to differentiate the flooded and non-flooded area was found as −21 dB when applying the Histogram thresholding method on the VH polarization dataset. The flood extent was increased (non-flood affected area was detected as a flood) when the threshold value was less than −21 dB. Whereas the actual flood affected area was missed when applying the threshold value on the histogram of signal backscatter intensity greater than −21 dB. Hence, determining an optimal threshold value is crucial to overcome both over and under estimation in flood inundation mapping. Due to the low viewing angle of the VV polarization, the optimal threshold was found at −15dB. However, increased false flood alarms were obtained when applying the threshold values less than the optimal (−15 dB).

A large difference in the overall accuracy of the flood map was obtained when using the VH (95%) and VV (86.7%) polarization data as input for the change detection method. The kappa coefficients of the two flood maps also showed a large difference (0.86 and 0.67), with VH resulting in a better agreement than VV in detecting surface flooded areas (Conde & De Mata Muñoz, 2019). This shows the importance of

evaluating the accuracy of the maps using the two polarizations before arbitrary selecting only one of the polarizations in multi-temporal flood mapping.

The RNID change detection method was better in flood detection than the histogram thresholding method for both VV and VH polarization data. The two methods resulted in an overall accuracy of 95% for RNID and 88% for the method of histogram thresholding. A large difference was also obtained in terms of the kappa statistics coefficient (0.86 for RNID and 0.71 for histogram thresholding). A widespread false flood affected area was detected on the north-east part of the catchment when applying the histogram thresholding method. We observed that the sandy soil areas and the agricultural land in that part of the catchment were moist but without any water impoundment. In Clement et al. (2017), a high amount of false flooded area was detected in areas where extensive agriculture was dominant in their study area. In the Akaki catchment, the flooded area that was detected by the histogram thresholding method was 5.17 times larger than the flooded area that was detected by the RNID change detection method using the same polarization of S-1 data.

Our finding indicates that the flood map accuracy for the RNID method slightly improved when the reference image was selected based on the comparison of candidate images in the dry season. Therefore, the best performing reference image (January 6, 2019) in applying the RNID was also found to be suitable for use for the entire analysis period (2017–2020).

The S-1 SAR images are acquired at 12 days interval in the Akaki catchment. Hence, not all flood events can be captured by the satellite. However, the flood maps generated from the satellite image proved to be useful information when long-time series multi-temporal images were analyzed as applied in this study. The risk of flood in the Akaki catchment has increased due to rapid urban expansion and climate change which requires further investigation (Birhanu et al., 2016). Future studies could monitor flooding in the Akaki catchment per 12 days interval using the S-1 images to provide useful information for flood risk assessment and management. Detailed feature characteristics, and assets exposed to and vulnerable to this flooding would be determined by combining the remote sensing satellite image and field survey for flood risk assessment (Risi et al., 2020). The flood extent detected from the S-1 dataset can be useful for validating hydrodynamic flood models of the study area.

The accuracy of the flood inundation map was successfully validated against the field data collected from a stretch of the floodplain area at the date of satellite overpass. We used actual GCPs collected from the field to reduce the accuracy deterioration that can occur with the use of secondary data as a reference. Future studies could investigate the scope of citizen science for community engagement in collecting GCPs for detailed flood characteristics (depth, location) at large (catchment) scale (Cheung and Feldman, 2019). However, the data reliability, motivation, engagement and experiences to deliver detailed flood extent information are challenges for the citizen science approach to flood monitoring (Sy et al., 2018). A flood that has a large depth and high velocity can also influence the citizen science approach since it can be life threatening. However, crowdsourced data gathered using electronic technologies (mobile devices), web platforms and installing staff gauges provide the opportunity to address these challenges and engage the citizen scientists for flood hazard monitoring (Le et al., 2016).

The change detection method applied in this study can be used to detect the flood affected area in the Awash River basin where the Akaki catchment is situated. The threshold and polarization selected for the Akaki catchment can be applied to the Awash River basin when the aim is rapid mapping of the flood extent. However, the confidence of the method can be increased by collecting GCPs from selected parts of the Awash River basin to apply a local training of the algorithm and evaluate the accuracy of the method. Flood mapping in other basins could repeat the method followed in this study to determine the most appropriate algorithm, polarization of the S-1 and threshold for detecting floods in comparable areas.

4. Conclusions

In this study, we evaluated the accuracy of Sentinel-1 VV and VH polarization data, and the histogram thresholding and Root of Normalized Image Difference for flood mapping in the Akaki catchment. Overall, the methods developed in this study could contribute to rapid flood exposure monitoring using the S-1 dataset. The following key conclusions have been drawn based on our analysis:

- The accuracy of the flood maps using the S-1 image was largely affected by image polarization, flood detection method, and reference image. Wet soils and low flood depths introduced additional errors in flood detection.
- The accuracy of the flood map was significantly higher using the VH polarization data rather than the VV polarization data.
- Flood inundation mapping of the Akaki catchment has a higher accuracy when generated using Root of Normalized Image Difference, instead of the histogram thresholding method. Thus, the Root of Normalized Image Difference method can be applied on the S-1 VH polarization dataset for monitoring flood inundation in the Akaki catchment.
- The reference image for the change detection method should be selected based on an accuracy assessment of the flood map.
- A multi-temporal analysis of S-1 images provides useful information on flood extent and frequency of occurrence in the Akaki catchment. The irrigated land was the most flood affected LULC class in terms of area coverage, but built-up and rain-fed agriculture were also affected. The S-1 image was found useful not only to identify flood affected LULC classes but also flood affected roads in the catchment. The built-up area and irrigated agricultural land that were highly affected with floods require further action to reduce the risk.

In this study, a single threshold value was applied to distinguish flooded and non-flooded area from the remote sensing images. Future studies could evaluate the merit of developing a local threshold value based on the LULC characteristics, soil characteristics and topography conditions. We highly recommended such an evaluation for large basins and heterogeneous catchments that are affected by flooding.

Declaration of competing interest

The authors have no conflict of interest to report.

Acknowledgment

References

Andreoli, R., Yesou, H., 2007. Large Scale Change Detection Techniques Dedicated to Flood Monitoring Using ENVISAT Wide Swath Mode Data.vol. 636, vol. 636. *European Space Agency, (Special Publication) ESA SP, SP*, pp. 1–6. https://doi.org/10.1109/IGARSS.2007.4423321.

Anusha, N., Bharathi, B., 2020. Flood detection and flood mapping using multi-temporal synthetic aperture radar and optical data. Egyptian Journal of Remote Sensing and Space Science 23 (2), 207–219. https://doi.org/10.1016/j.ejrs.2019.01.001.

Bayik, C., Abdikan, S., Ozbulak, G., Alasag, T., Aydemir, S., Sanli, F.B., 2018. Exploiting multi-temporal Sentinel-1 SAR data for flood extend mapping. Int. Archives Photogrammetry Remote Sensing Spatial Inf. Sci. ISPRS Archives 42 (3W4), 109–113. https://doi.org/10.5194/isprs-archives-XLII-3-W4-109-2018.

Bhatt, C.M., Rao, G.S., Farooq, M., Manjusree, P., Shukla, A., Sharma, S.V.S.P., Kulkarni, S.S., Begum, A., Bhanumurthy, V., Diwakar, P.G., Dadhwal, V.K., 2017. Satellite-based assessment of the catastrophic jhelum floods of September 2014, jammu & Kashmir, India. Geomatics, Nat. Hazards Risk 8 (2), 309–327. https://doi.org/10.1080/19475705.2016.1218943.

Birhanu, D., Kim, H., Jang, C., Park, S., 2016. Flood risk and vulnerability of Addis Ababa city due to climate change and urbanization. Procedia Eng. 154, 696–702. https://doi.org/10.1016/j.proeng.2016.07.571.

Cheung, W., Feldman, D., 2019. Can citizen science promote flood risk communication? Water (Switzerland) 11 (10), 1–9. https://doi.org/10.3390/w11101961.

Chini, M., Pelich, R., Pulvirenti, L., Pierdicca, N., Hostache, R., Matgen, P., 2019. Sentinel-1 InSAR Coherence to Detect Floodwater in Urban Areas : Houston and Hurricane Harvey as A Test Case, pp. 1–20.

Clement, M., Kilsby, C., Moore, P., 2017. Multi-Temporal SAR Flood Mapping using Change Detection Multi-temporal synthetic aperture radar flood mapping using change detection. J. Flood Risk Manag. 11 (2), 152–168. https://doi.org/10.1111/jfr3.12303.

Conde, F.C., De Mata Muñoz, M., 2019. Flood monitoring based on the study of Sentinel-1 SAR images: the Ebro River case study. Water (Switzerland) 11 (12), 1–25. https://doi.org/10.3390/w11122454.

Dadhich, G., Miyazaki, H., Babel, M., 2019. Applications of sentinel-1 synthetic aperture radar imagery for floods damage assessment: a case study of nakhon si thammarat, Thailand. Int. Archives Photogrammetry Remote Sensing Spatial Inf. Sci. ISPRS Archives 42 (2/W13), 1927–1931. https://doi.org/10.5194/isprs-archives-XLII-2-W13-1927-2019.

Demlie, M., Wohnlich, S., Gizaw, B., Stichler, W., 2007. Groundwater recharge in the Akaki catchment, central Ethiopia : evidence from environmental isotopes (d 18 O , d 2 H and 3 H) and chloride mass balance. Hydrol. Process. 21, 807–818. https://doi.org/10.1002/hyp.6273.

Devries, B., Huang, C., Armston, J., Huang, W., Jones, J.W., Lang, M.W., 2020. Remote sensing of environment rapid and robust monitoring of flood events using sentinel-1 and Landsat data on the Google earth engine. Remote Sens. Environ. 240, 111664. https://doi.org/10.1016/j.rse.2020.111664. October 2018.

Ganji, K., Gharachelou, S., Ahmadi, A., 2019. Urban'S river flood analysing using sentinel-1 data case study: (Gorganrood, Aq'Qala). ISPRS - Int. Archives Photogramm. Remote Sensing Spatial Inf. Sci. https://doi.org/10.5194/isprs-archives-xlii-4-w18-415-2019. XLII-4/W18(October), 415–419.

Gumma, M.K., Amede, T., Getnet, M., Pinjarla, B., Panjala, P., Legesse, G., Tilahun, G., Van Den Akker, E., Berdel, W., Keller, C., Siambi, M., Whitbread, A.M., 2020. Assessing Potential Locations for Flood-Based Farming Using Satellite Imagery: A Case Study of Afar Region, Ethiopia. Renewable Agriculture and Food Systems. https://doi.org/10.1017/S1742170519000516.

Hostache, R., Matgen, P., Wagner, W., 2012. Change detection approaches for flood extent mapping: how to select the most adequate reference image from online archives? Int. J. Appl. Earth Obs. Geoinf. 19 (1), 205–213. https://doi.org/10.1016/j.jag.2012.05.003.

Kianfar, N., 2019. The Applicability of Dual Polarized SENTINEL-1 SAR Data for Detection of Flooded Areas in Pol-E Dokhtar, Lorestan, Iran, pp. 12–14. XLII(October).

Le, J., Patalano, A., Collins, D., Federico, N., Marcelo, C., Smart, G.M., Bind, J., Chiaverini, A., Le, R., Dramais, G., Braud, I., 2016. Crowdsourced data for flood hydrology : feedback from recent citizen science projects in Argentina , France and New Zealand. J. Hydrol. https://doi.org/10.1016/j.jhydrol.2016.07.036.

Li, Y., Martinis, S., Plank, S., Ludwig, R., 2018a. An automatic change detection approach for rapid flood mapping in Sentinel-1 SAR data. Int. J. Appl. Earth Obs. Geoinf. 73, 123–135. https://doi.org/10.1016/j.jag.2018.05.023. May.

Li, Y., Martinis, S., Wieland, M., Schlaffer, S., Natsuaki, R., 2019. Urban flood mapping using SAR intensity and interferometric coherence via Bayesian network fusion. Rem. Sens. 11 (19). https://doi.org/10.3390/rs11192231.

Liang, J., Liu, D., 2020. A local thresholding approach to flood water delineation using Sentinel-1 SAR imagery. ISPRS J. Photogrammetry Remote Sens. 159, 53–62. https://doi.org/10.1016/j.isprsjprs.2019.10.017. February 2019.

Long, S.A., Fatoyinbo, T.E., Frederick, P., 2014. Simplified change detection method for flood extent mapping using SAR. Environ. Res. Lett. 9. December.

Manjusree, P., Prasanna Kumar, L., Bhatt, C.M., Rao, G.S., Bhanumurthy, V., 2012. Optimization of threshold ranges for rapid flood inundation mapping by evaluating

backscatter profiles of high incidence angle SAR images. Int. J. Disaster Risk Sci. 3 (2), 113–122. https://doi.org/10.1007/s13753-012-0011-5.

Martinis, S., Plank, S., 2018. The Use of Sentinel-1 Time-Series Data to Improve Flood Monitoring in Arid Areas, vol. 1. https://doi.org/10.3390/rs10040583.

Mason, D.C., Dance, S.L., Cloke, H.L., 2021. Floodwater detection in urban areas using Sentinel-1 and WorldDEM data. https://doi.org/10.1117/1.JRS.15.032003, 15,3,1-22.

Mutanga, O., Kumar, L., 2019. Google earth engine applications. Rem. Sens. 11 (5), 11–14. https://doi.org/10.3390/rs11050591.

Nguyen, H.T.T., Doan, T.M., Tomppo, E., McRoberts, R.E., 2020. Land use/land cover mapping using multitemporal sentinel-2 imagery and four classification methods-A case study from Dak Nong, Vietnam. Rem. Sens. 12 (9), 1–28. https://doi.org/10.3390/RS12091367.

Nkomeje, F., 2017. Comparative Performance of Multi-Source Reference Data to Assess the Accuracy of Classified Remotely Sensed Imagery : Example of Landsat 8 OLI across Kigali City-Rwanda 2015 Felicien Nkomeje to Cite This Version : HAL Id : Hal-01455461 Comparative Perform.

O'Hara, R., Green, S., McCarthy, T., 2019. The agricultural impact of the 2015-2016 floods in Ireland as mapped through Sentinel 1 satellite imagery. Ir. J. Agric. Food Res. 58 (1), 44–65. https://doi.org/10.2478/ijafr-2019-0006.

Pekel, J.F., Cottam, A., Gorelick, N., Belward, A.S., 2016. High-resolution mapping of global surface water and its long-term changes. Nature 540 (7633), 418–422. https://doi.org/10.1038/nature20584.

Reksten, J.H., Solberg, R., 2019. Flood detection in Norway based on sentinel-1 sar imagery. Int. Archives Photogrammetry Remote Sensing Spatial Inf. Sci. ISPRS Archives 42 (3/W8), 349–355. https://doi.org/10.5194/isprs-archives-XLII-3-W8-349-2019.

Risi, R. De, Jalayer, F., Paola, F. De, Carozza, S., 2020. From flood risk mapping toward reducing vulnerability : the case of Addis Ababa. Nat. Hazards 100 (1), 387–415. https://doi.org/10.1007/s11069-019-03817-8.

Rwanga, S.S., Ndambuki, J.M., 2017. Accuracy assessment of land use/land cover classification using remote sensing and GIS. Int. J. Geosci. 611–622. https://doi.org/10.4236/ijg.2017.84033, 08(04).

Schlaffer, S., Matgen, P., Hollaus, M., Wagner, W., 2015. Flood detection from multi-temporal SAR data using harmonic analysis and change detection. Int. J. Appl. Earth Obs. Geoinf. 38, 15–24. https://doi.org/10.1016/j.jag.2014.12.001.

Surampudi, S., Yarrakula, K., 2019. Mapping and assessing spatial extent of floods from multitemporal synthetic aperture radar images: a case study on Brahmaputra River in Assam State, India. Environ. Sci. Pollut. Control Ser. https://doi.org/10.1007/s11356-019-06849-6.

Sy, B., Frischknecht, C., Dao, H., 2018. Flood Hazard Assessment and the Role of Citizen Science. https://doi.org/10.1111/jfr3.12519. January 2020.

Tavus, B., Kocaman, S., Gokceoglu, C., Nefeslioglu, H.A., 2018. Considerations on the Use of SENTINEL-1 Data in Flood Mapping in Urban Areas: Ankara (turkey) 2018 Floods, pp. 20–23. XLII(November).

Trigg, M.A., Michaelides, K., Neal, J.C., Bates, P.D., 2013. Surface water connectivity dynamics of a large scale extreme flood. J. Hydrol. 505, 138–149. https://doi.org/10.1016/j.jhydrol.2013.09.035.

Tsyganskaya, V., Martinis, S., Marzahn, P., Ludwig, R., 2018. Detection of temporary flooded vegetation using Sentinel-1 time series data. Rem. Sens. 10 (8). https://doi.org/10.3390/rs10081286.

Verde, N., Kokkoris, I.P., Georgiadis, C., Kaimaris, D., 2020. National Scale Land Cover Classification for Ecosystem Services Mapping and Assessment , Using Multitemporal Copernicus EO Data and Google Earth Engine.

Zeng, Z., Gan, Y., Kettner, A.J., Yang, Q., Zeng, C., Brakenridge, G.R., 2020. Towards high resolution fl ood monitoring : an integrated methodology using passive microwave brightness temperatures and Sentinel synthetic aperture radar imagery. J. Hydrol. 582, 124377. https://doi.org/10.1016/j.jhydrol.2019.124377. May 2019.

Zhang, M., Chen, F., Liang, D., Tian, B., Yang, A., 2020. Use of sentinel-1 GRD SAR images to delineate flood extent in Pakistan. Sustainability 12 (14), 5784. https://doi.org/10.3390/su12145784.